2021

Impact of Neutron Energy on Asteroid Deflection Performance

Lansing S. Horan IV

Darren E. Holland

Megan Bruck Syal
Lawrence Livermore National Laboratory

James E. Bevins
Air Force Institute of Technology

Joseph W. Wasem
Lawrence Livermore National Laboratory

Recommended Citation

Horan, L. S., Holland, D. E., Bruck Syal, M., Bevins, J. E., & Wasem, J. V. (2021). Impact of neutron energy on asteroid deflection performance. Acta Astronautica, 183, 29–42. https://doi.org/10.1016/j.actaastro.2021.02.028

Acta Astronautica 183 (2021) 29–42

Contents lists available at ScienceDirect

Acta Astronautica

journal homepage: www.elsevier.com/locate/actaastro

Research paper

Impact of neutron energy on asteroid deflection performance ☆

Lansing S. Horan IV [a,*], Darren E. Holland [a], Megan Bruck Syal [b], James E. Bevins [a], Joseph V. Wasem [b]

[a] Air Force Institute of Technology, 2950 Hobson Way, WPAFB, OH 45433, USA
[b] Lawrence Livermore National Laboratory, P.O. Box 808, Livermore, CA 94550, USA

ARTICLE INFO

Keywords:
NEO nuclear deflection/mitigation
Loosely coupled radiation hydrodynamics
Energy deposition profile
Energy coupling efficiency
Blow-off momentum impulse
Asteroid planetary defense

ABSTRACT

In the future, a hazardous asteroid will find itself on a collision course with Earth. For asteroids of moderate size or larger, a nuclear device is one of humanity's only technologies capable of mitigating this threat via deflection on a timescale of less than a decade. This work examined how the output neutron energy from a nuclear device standoff detonation affects the deflection of a notional asteroid that is 300 meters in diameter and composed of silicon dioxide at a bulk density of 1.855 g/cm^3. 14.1 MeV and 1 MeV neutron energy sources were modeled in MCNP to quantify the energy deposition in the asteroid target. The asteroid's irradiated region was discretized in angle by tracing the rays emanating from the point of detonation and in depth by considering the neutron mean-free-paths. This high-fidelity approach was shown to deviate from previous analytic approximations commonly used for asteroid energy deposition. 50 kt and 1 Mt neutron yields of the energy deposition mappings were imported into a hydrodynamic asteroid model in ALE3D to simulate the deflective response due to blow-off ejecta. Underexplored in literature, changing the neutron energy was found to have up to a 70% impact on deflection performance due to induced differences in the energy deposition profile and in the energy coupling efficiency. The magnitude of energy deposition accounted for most of the observed variation in the asteroid velocity change, making the coupling efficiency more significant than the spatial profile characteristics. These findings are vital for determining the optimal source neutron energy spectrum for asteroid deflection applications.

1. Background and introduction

Asteroid collisions with Earth can be entirely unnoticed or apocalyptic, and everywhere in-between. The impact devastation to be expected depends primarily on the size of the incident asteroid — the more massive the object, the greater the potential damage [2]. Fortunately, asteroids in our solar system follow an approximate power-law size distribution: the smallest asteroids are orders of magnitude more abundant than very large asteroids [3].

Of particular interest and concern are asteroids that fall in the near-Earth object (NEO) and especially the potentially hazardous object (PHO) categorizations. A NEO is "an asteroid or comet that comes within 1.3 astronomical units (au) of the Sun," where Earth's average orbit is defined as the 1.0 au standard [4]. A PHO satisfies the following two criteria: (1) the body approaches Earth at a distance of 0.05 au (7.5 million kilometers) or closer, and (2) the object is at least 140 meters or greater in diameter [4]. When the NEO and/or PHO is an asteroid, the terms NEA (near-Earth asteroid) and PHA (potentially hazardous asteroid) are also used.

As of 1 October 2020, 9,336 NEAs with diameters greater than 140 m have been discovered, and of these, 2,122 are classified as PHAs [5]. Analysis in past work estimated that there are ~27,100 ± 2,200 total 140+ m NEAs in existence [6], meaning that approximately 34.5% ± 2.8% of these asteroids have been found up to and through September 2020. A single asteroid of this size – where the family of 140+ m NEAs collectively has about a 1% chance of one member hitting Earth per 100-year period [7] – would release approximately 100+ megatons (Mt) of TNT-equivalent to Earth, presenting a severe-damage risk at the regional level. This devastating amount of energy from such an asteroid collision would well surpass the 50 Mt yield of the "Tsar Bomba" Soviet nuclear device, which remains the largest nuclear explosion in history [8].

☆ This publication heavily expands, revises, and improves upon a conference report [1] that was submitted to, and presented in, the 2020 IEEE Aerospace Conference in Big Sky, MT, USA. This journal paper largely supersedes the prior preliminary work from the same authors.

* Correspondence to: Air Force Technical Applications Center, 1020 South Patrick Drive, BLDG 10989, Patrick SFB, FL 32925, USA (author's current affiliation).
E-mail addresses: lansing.horan@aggienetwork.com (L.S. Horan IV), Darren.Holland@afit.edu (D.E. Holland), syal1@llnl.gov (M.B. Syal), James.Bevins@afit.edu (J.E. Bevins), wasem2@llnl.gov (J.V. Wasem).

https://doi.org/10.1016/j.actaastro.2021.02.028
Received 10 October 2020; Received in revised form 17 February 2021; Accepted 23 February 2021
Available online 4 March 2021

The magnitude of damage that could result from these fairly-rare, one-off asteroid impact events makes the planetary defense mission a prudent pursuit. While an array of technologies have been proposed to mitigate hazardous asteroids [9–11], nuclear explosives are the most effective and efficient means of deflecting these objects. In fact, NASA found that nuclear standoff explosions are 10–100 times more effective than non-nuclear alternatives for diverting an asteroid [9]. A nuclear device is by-far the most mass-efficient technology for storing and delivering usable energy – nuclear energy densities are nearly one million times greater than what chemical bonds can store [12] – an important practical consideration given the payload constraints of rockets when launching material into space [13]. This ability to deliver such an abundance of energy also pays off by shortening the mitigation timeline; a nuclear device is one of the only viable options for mitigating an incoming 140+ m asteroid on a less than decadal timescale. Indeed, in scenarios where there is little warning time prior to impact and/or where the incident asteroid is large, a nuclear device might be the only practical option [14]. The outputs and effects of nuclear explosions are well characterized; nuclear devices are a mature technology [15]. All of these factors make the nuclear option a prime choice for combating asteroids on a collision path with Earth.

There are two ways to apply nuclear explosives to defeat an asteroid: disruption and deflection. Disruption is the act of fragmenting or pulverizing the asteroid into a field of high-velocity debris [16], whereby >99.5% of the original body's mass never reaches Earth, even for very late warning times (less than a month prior to impact) [13]. Deflection is the gentler approach of pushing the asteroid onto a new trajectory, slightly changing its velocity while keeping the object intact [13]. In this way, so long as the velocity change δV is great enough, then over a few years of time this integrates to an Earth-missing deflection distance, and the fated collision is avoided entirely. All things being equal, deflection would likely be preferred over disruption. Deflection is generally considered to be the safer and more "elegant" approach [15]. Thus, this paper studies the nuclear deflection option.

Detonating a nuclear device above an asteroid irradiates a certain surface area. Much of the material near the surface of this region is nearly-instantly melted and/or vaporized by the rapid energy deposition from prompt x-rays, neutrons, and gamma rays. Subsequently, this relatively small amount of superheated material expands away from the asteroid as "blow-off", inducing a pressure wave in the remaining majority asteroid body. Thus, a rocket-like exhaust momentum impulse is imparted over a very short time, and as a result the asteroid's original velocity V is changed by some δV, thereby deflecting the asteroid [13,15,17].

In this work, neutrons are the only form of radiation output considered from a nuclear detonation, because neutrons are generally the most penetrative and therefore the most effective source type for deflection [14]. This is *not* intended to suggest that extant nuclear devices which principally produce x-rays are somehow unproductive against asteroids. It is well established that x-ray yields can be efficacious across a broad range of asteroid scenarios [18]. Nevertheless, because neutron-producing devices can perform at even higher efficiency levels, this work focuses on the neutron portion.

In much of the published literature involving asteroid nuclear deflection simulations, the neutron source component is simply assumed to be either the Watt fission spectrum [19] or fusion reaction energies, such as mono-energetic 2.45 MeV [14] or 14.1 MeV [20] neutrons. However, to the authors' knowledge, there is little-to-no published research exploring neutron source energies in a comparative lens, so as to determine which neutron energies are best for asteroid deflection.

Previous work on *disruption* involved preliminary hydrodynamics simulations which suggested that "the spatial variations in energy deposition in an asteroid can have a significant effect on the resulting degree of disruption" [21]. If the surface energy deposition profiles vary strongly with the neutron energy, then perhaps this will also have an effect in *deflective* scenarios. A prior study on deflection tentatively found that lower-energy neutrons might convert a greater fraction of their initial deposited energy into useful kinetic energy in an asteroid, meaning that the deflection velocity was increased [22]. This hypothesis suggests that fission (lower-energy) neutrons might be more ideal for deflection than fusion (high-energy) neutrons, with respect to this "kinetic" coupling.

A 2010 letter from the Office of Science and Technology Policy to the U.S. Congressional Committee on Science and Technology asserted that "significantly more analysis and simulation [is] needed" in the arenas of asteroid mitigation and deflection [23]. Bruck Syal et al. noted that "[r]elatively little quantitative assessment of nuclear deflection has been conducted" and that "[t]here remains much work to determine the optimal use of nuclear explosives against large bodies" [13]. For application in asteroid mitigation, Dearborn remarked that the "optimal type of device may not be in any nation's stockpile" [24]. This paper is a step towards determining both the optimal device for asteroid defeat and the type of simulation methodology that can evaluate nuclear deflection performance.

2. Case studies and approach

Two neutron energies[1] – 14.1 MeV from deuterium–tritium fusion [26] and 1 MeV from near the Watt fission peak [27] – are studied at two neutron yields – 50 kt and 1 Mt – radiating from a fixed standoff point above an asteroid target. The resulting asteroid velocity change, δV, is determined for each configuration. The set of results are compared in order to illumine how variations in energy deposition spatial profiles and energy coupling efficiencies – the two principal qualities of energy deposition, both of which change with the source neutron energy – can affect the asteroid deflection performance.

The notional asteroid target in this work is spherical, 300 m in diameter, and composed of silicon dioxide with a porosity of 0.30, resulting in a bulk density of 1.855 g/cm^3. The Apophis-sized body, such as this asteroid, has been considered as "near the boundary" where non-nuclear kinetic impactor missions would become "heroic" and nuclear deflection would be the more practical choice [13]. While real asteroid compositions will consist of a variety of mineral assemblages, silicon dioxide (SiO_2) is a reasonable surrogate material. Previous work has shown that deflection response is similar for a variety of silicate minerals [18]. In addition, SiO_2 is a well-studied and well-defined material, being a major component of terrestrial rocks. A 30% porosity is selected because the resulting bulk material density is close to 2 g/cm^3, a value typical of the asteroid densities that have been measured [28].

There are two phases to this research: (1) neutron energy deposition, and (2) asteroid deflective response. First, version 6.2 of Monte Carlo N-Particle (MCNP), a general-purpose Monte Carlo radiation transport code from Los Alamos National Laboratory (LANL) [29], was used to obtain high-fidelity neutron energy deposition profiles in the asteroid target. Nuclear cross sections for interaction probabilities were obtained from the U.S. Evaluated Nuclear Data Library B-VII.1 [30]. Second, the MCNP-generated energy deposition spatial profiles served as inputs to initialize a hydrodynamic transport asteroid simulation and thereby quantify the δV deflection. Version 4.30.29 of ALE3D, a two- and three-dimensional Arbitrary Lagrangian–Eulerian (ALE) hydrodynamics code developed by Lawrence Livermore National Laboratory (LLNL) [31], was used.

[1] The "14.1 MeV" source is the DPLUS energy group #3 uniformly sampled between the bin boundaries of 13.840 MeV and 14.191 MeV, and the "1 MeV" source is group #21 from 0.96164 MeV to 1.1080 MeV. In this paper, these sources will be referred to as 14.1 MeV and 1 MeV respectively because the midpoint or average energy for each group is quite close to these values. The DPLUS group structure is based on the DABL69 library, which has been used in radiation shielding problems in defense applications [25].

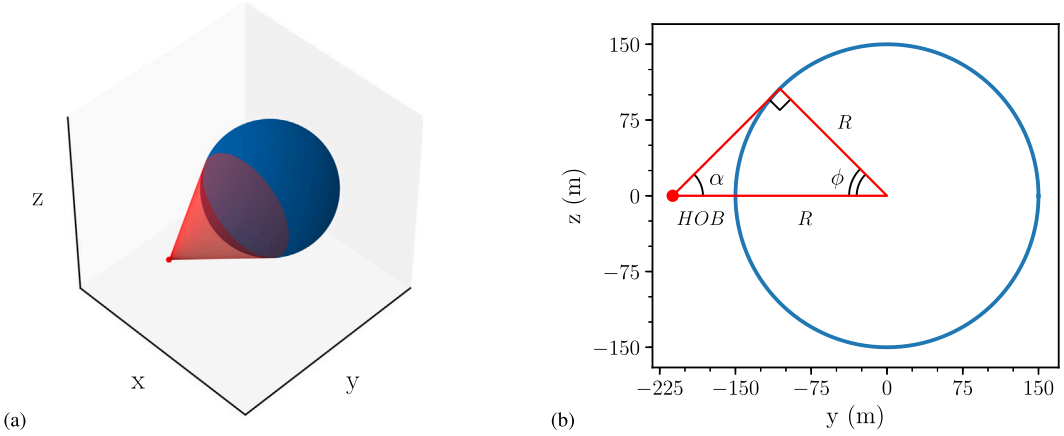

Fig. 1. 3-D and 2-D views of the device-asteroid geometry. (a) The asteroid coordinate system visualizes the fraction of nuclear radiation (red cone) that is incident on the asteroid (blue sphere) from a device detonation (red point) at a fixed standoff distance from the asteroid surface. (b) The encounter geometry side-view shows α as the device-centered half-angle and ϕ as the asteroid-centered half-angle. R is the asteroid radius and HOB is the height-of-burst of the nuclear device. (For interpretation of the references to color in this figure legend, the reader is referred to the web version of this article.)

This paper is divided into the major sections that follow: Section 3 defines the standoff distance and details the spatial discretization procedure, Section 4 states the MCNP setup, Section 5 provides the results and analysis of the MCNP energy deposition simulations, Section 6 states the ALE3D setup, Section 7 provides the results and analysis of the ALE3D asteroid deflection simulations, and Section 8 summarizes the overall findings from these efforts.

3. Problem geometry

3.1. Device standoff distance

Fig. 1a shows the 3-D Cartesian coordinate system defined in this work. The asteroid (blue sphere) of radius R is centered at the origin $(0, 0, 0)$. The standoff distance, or height-of-burst (HOB), of the nuclear device can be expressed as a scaled asteroid radius [1],

$$HOB = cR, \tag{1}$$

where c is a non-dimensional sizing factor. The nuclear device (red point) located at position $(0, -(R + HOB), 0)$ is treated as an isotropic neutron point-source, which is a reasonable approximation given the asteroid size (300 m) compared to a nuclear device (on the order of a few meters).

The angular and spatial conventions are defined as in Fig. 1b, borrowing from the style of Hammerling and Remo [32]. The half-angle α denotes the fraction of radiation from the detonation that is incident on the asteroid surface, while ϕ is the half-angle representing the fraction of the asteroid surface area that is irradiated. Using Eq. (1), it follows that

$$\sin\alpha = \frac{R}{R + HOB} = \frac{R}{R + cR} = \frac{1}{1 + c} \tag{2}$$

and

$$\phi = \frac{\pi}{2} - \alpha. \tag{3}$$

Eqs. (2) and (3) show that the energy fraction α and the surface area fraction ϕ are functions only of the HOB scaling factor c.

The fixed standoff distance examined in this work is $c = \sqrt{2} - 1 \approx 0.414$, which is the "optimal" HOB derived by Hammerling and Remo [32]. This is the distance where the sum of two fractions, the fraction f of the asteroid surface area irradiated and the fraction g of the device yield that reaches the asteroid target, is maximized. This standoff distance from the asteroid is the geometrical optimum because it balances the trade-offs: it is where both $\alpha = 45°$ and $\phi = 45°$. For the 150 m asteroid radius, the standoff distance at $c \approx 0.414$ is ~62.13 m.

Table 1
Microscopic cross sections σ of ^{28}Si and ^{16}O for 14.1 MeV and 1 MeV neutrons, alongside the neutron mean-free-paths λ in SiO_2.

E_n	Nuclide	σ	λ
14.1 MeV	^{28}Si	1.81 b	10.8 cm
	^{16}O	1.59 b	
1 MeV	^{28}Si	4.68 b	2.6 cm
	^{16}O	8.15 b	

Note that this geometric optimum is *not necessarily* identical to the "true optimal" HOB, or the standoff distance that would maximize the momentum impulse and therefore the δV velocity change for asteroid deflection. The true optimal standoff distance is situation-specific and likely depends on several parameters, including the asteroid's composition, structure, and geometry, along with the maximum available yield and outputs of the nuclear device, and likely even the resulting energy deposition spatial profiles.

3.2. Asteroid spatial discretization

A unique discretization methodology was developed to efficiently tally the energy deposition spatially across the asteroid's region of irradiation. In brief, the selected resolution in the radial direction was informed by the neutron mean-free-path (MFP). In the angular direction, the resolution was determined by how the asteroid curvature affects a fixed penetration depth via ray-tracing. This subsection serves to explain and visualize the spatial discretization procedure.

The MFP λ is the expected distance that a neutron will travel on average before colliding with a nuclei and interacting [33]:

$$\lambda = \frac{1}{\frac{\rho N_A}{M}\sigma}, \tag{4}$$

where ρ is the material density, N_A is Avogadro's number, M is the molecular weight of the material (~60 g/mol for SiO_2), and σ is the microscopic cross section. Using the known σ values for 14.1 MeV and 1 MeV neutrons interacting with ^{28}Si and ^{16}O (the predominate constituents of SiO_2) [30], Table 1 displays the respective λ MFPs in SiO_2.

The MFPs of a few centimeters implied that the spatial resolution in the asteroid should be on the order of centimeters – and perhaps even millimeters at the outer surface – in the radial (depth) direction. This was required to properly capture the detail in the energy deposition profiles. In addition, for reasonable neutron yields, preliminary MCNP trials determined that neutron energy deposition was only significant

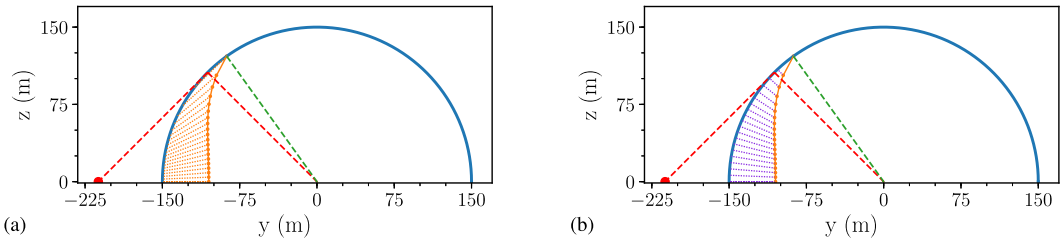

Fig. 2. Neutron penetration depths in the device and asteroid frames of reference. (a) The device-centered 4.5 m penetration depths (dashed orange lines; exaggerated here to 45 m) are ray-traced for all α angles into the asteroid target. (b) These depths are converted to the asteroid-centered depths d_{NEO} (purple dashed lines) as referenced to the ϕ angles pointing towards the asteroid core. From the burst at $c \approx 0.414$ standoff, the dashed red lines bound both the $\alpha = 45°$ energy fraction that intercepts the target and the $\phi = 45°$ irradiated asteroid surface area. The dashed green lines show the slight extension of ϕ up to ϕ' to capture the neutron rays at the periphery. (For interpretation of the references to color in this figure legend, the reader is referred to the web version of this article.)

up to ~4.5 m beneath the surface. Not only was this problem poorly-scaled in terms of depth, but the spherical asteroid geometry made typical Cartesian meshing both undesirable and impractical. Also, from *a priori* intuition and previous work, it was unclear how to adequately partition the angular direction and what resolution would be necessary.

These issues were solved by the development and application of a ray-tracing procedure along the asteroid curvature. Instead of Cartesian meshing, a conical- and spherical-based meshing pattern was created for angular and radial discretizations at appropriate refinements. For Figs. 2, 3, and 4, the maximum penetration depth is exaggerated by a factor-of-ten to 45 m, rather than the actual 4.5 m maximum depth tallied in the upcoming MCNP simulations. This makes the discretization procedure easily visible on the 300 m asteroid scale. Also, for this same purpose of providing a visual example, the resolutions of the angular and radial discretizations have been greatly decreased.

Neutrons radiating from the device will intersect the asteroid surface over a range of angles from the source, from 0° up to α (see Eq. (2) and Fig. 1b). At the 0° angle, a neutron hits ground zero (GZ) exactly on the asteroid surface. At this angle, it may penetrate up to 4.5 m beneath this surface. At all other angles greater than 0° and less than α, a neutron's path is incident upon the asteroid surface at a non-normal angle. As such, the constant 4.5 m maximum target depth must be translated to match the shifting angles of incidence of the neutrons emanating from the device. Using circle-line intersection equations and trigonometric relations [34], a ray-tracing procedure was performed. Discrete incidence angles were selected to cover the span from 0° up to α, and along each ray, the same 4.5 m depth was projected into the asteroid (orange dashed lines in Fig. 2a). This traced the deepest positions into the asteroid target where energy deposition would be significant, as a function of the incidence angle. The ray-tracing calculations of the maximum depths resulted in the orange points beneath the asteroid surface in Fig. 2a. This line of data points extended slightly beyond the outer surface area that is directly irradiated by the device (red dashed lines). To capture the entire energy deposition region out to 4.5 m depths, the asteroid-centered ϕ was slightly increased to ϕ' (green dashed lines) to also encompass this small edge region near the surface.

The conversion of device-centered 4.5 m depths to asteroid-centered penetrations forms the foundation for both the angular and the radial discretizations. The distance between each orange point in Fig. 2a and the center of the asteroid (i.e. the Euclidean L2-norm) was subtracted from the asteroid radius. Thus, the asteroid-centered penetration depths, or d_{NEO} (which stands for "depth into the NEO"), were calculated as a function of the asteroid-centered ϕ. The magnitudes of d_{NEO} are shown by the lengths of the purple dashed lines in Fig. 2b. As expected at the 0° angle through GZ, the asteroid-centered penetration depth in Fig. 2b is the same as the device-centered penetration depth in Fig. 2a. At all other angles, however, the asteroid-centered d_{NEO} decreases as ϕ increases.

In Fig. 3, the d_{NEO} magnitudes (lengths of the purple dashed lines in Fig. 2b) are now shown as purple points at the sampled ϕ angles.

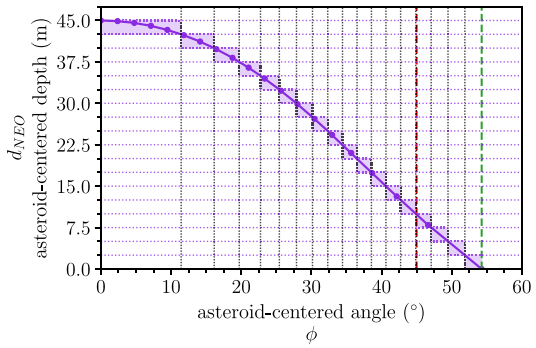

Fig. 3. Angular discretization of the asteroid's irradiated region where energy is deposited. The asteroid-centered penetration depth d_{NEO} is a function of asteroid-centered angle ϕ, from 0° at GZ up to the maximum ϕ' from the ray-tracing procedure. The angular discretization (vertical black dashed lines) is dependent on the Δd_{NEO} tolerance: the constant spacing between the horizontal purple dashed lines of 0.875 cm (exaggerated here as 2.5 m for viewing purposes). Each purple-shaded box encloses the divisions in d_{NEO} and ϕ along the non-linear d_{NEO} curve. (For interpretation of the references to color in this figure legend, the reader is referred to the web version of this article.)

A piecewise linear interpolation function (the solid purple line) was fit to the discrete (ϕ, d_{NEO}) points to obtain a complete d_{NEO} curve across the span in ϕ. The d_{NEO} radial space was divided into equally-tall blocks of height Δd_{NEO}, seen by the constant spacing between the horizontal purple dashed lines in Fig. 3. The intersections of these horizontal dividing lines with the d_{NEO} curve determined how the ϕ angular space should be discretized (the vertical black dashed lines). In effect, each angular bin resulting from this type of discretization groups reasonably-similar neutron penetration depths together. For the MCNP simulations, the Δd_{NEO} tolerance was 0.875 cm, a value less than the MFPs for MeV-level neutrons as in Table 1. Starting with the maximum 4.5 m penetration depth at GZ, following the d_{NEO} curve all the way down to 0 at the periphery – in steps of Δd_{NEO} – resulted in 515 angular divisions spanning $\phi = 0°$ to $\phi = \phi'$.

This approach to divisioning allows for higher angular resolution where the maximum penetration depth changes more quickly. Smaller angular bins in certain locations ensure that the more rapid angular variations are not lost by excessive spatial averaging. As seen in Fig. 3, this d_{NEO} curve changes more quickly as ϕ increases. Because the discretization is tied to the d_{NEO} curve itself, greater angular resolution is automatically achieved where it is needed. This system of discretization should efficiently capture the angular gradients of the energy deposition profiles.

Fig. 4a shows the angular dividing lines in the YZ-plane side-view. For an isotropic point-source radiating towards a spherical body, the y-axis is an axis of symmetry (see Fig. 1). To exploit this symmetry, the discretization in Fig. 4a was rotated 360° about the y-axis (i.e. the z = 0 line), forming conical surfaces from the angular divisions. Fig. 4b

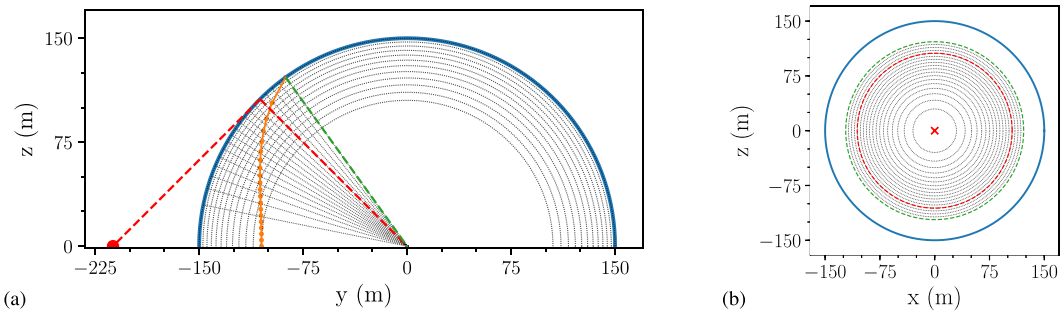

Fig. 4. The angular and radial discretization visualized in the observer's "side-view" and the device's "front-view". (a) The YZ-plane side-view depicts the finalized discretization scheme (dashed black lines): encapsulated cones for the angular direction and concentric spherical shells in the radial direction. The concentric spherical surfaces are logarithmically-spaced: the resolution is highest at the outer surface and gradually relaxed as the depth increases. (b) The XZ-plane front-view shows the circular bases of the encapsulated cones intersecting the spherical asteroid surface. The neutrons radiate from the point of detonation (red X) towards the asteroid target (into the page). (For interpretation of the references to color in this figure legend, the reader is referred to the web version of this article.)

shows the circular bases of these cones intersecting the asteroid's outer surface in the XZ-plane front-view. This perspective shows the surface area of the asteroid target as seen by the standoff nuclear device. This symmetric, cone-based angular discretization allowed the 3-D asteroid geometry to be converted into a 2-D (d_{NEO} and ϕ) energy deposition problem, greatly reducing the number of necessary computations.

While the angular discretization was determined by how the asteroid curvature affects a fixed penetration depth, the radial discretization was informed by the neutron MFP. Because the MFPs of 14.1 MeV and 1 MeV neutrons are on the order of several centimeters (see Table 1), the energy deposition was expected to change on a centimeter- or even millimeter-scale beneath the surface. Because most of the neutron energy was to be deposited near the asteroid surface, logarithmically-spaced concentric spherical shells were generated between the outer surface and the maximum 4.5 m depth. For the MCNP simulations, the finest resolution between the shells was 0.5 mm at the surface, which was logarithmically increased up to the broadest 4 cm at the 4.5 m mark beneath the surface. This resulted in 498 total shells throughout the $d_{NEO} \in [0, 4.5]$ m radial space. Fig. 4a shows only 11 spherical surfaces with very-large spacing to demonstrate this type of radial discretization.

4. MCNP methodology

The correct energy deposition input is essential for correctly modeling the resulting asteroid deflection. If large uncertainties in the energy deposition values exist, or if the spatial refinement is too coarse to smoothly capture the heating gradients, there should be minimal confidence in the subsequent hydrodynamic asteroid response. MCNP was used to explore the characteristics of neutron energy deposition at and beneath the asteroid's surface.

4.1. MCNP input deck setup

A 3-D representation of the asteroid was modeled in MCNP with conical and spherical divisions in the angular and radial directions, as corresponding to the axisymmetric 2-D discretization shown in Fig. 4a. The detonation was modeled as an isotropic point-source. However, only the neutrons released within the α half-angle will ever collide with the asteroid. At the $c \approx 0.414$ HOB, approximately 14.64% of the neutrons spewing from the point of detonation are emitted towards the asteroid surface; the rest of the output neutrons (and their energies) are lost to the void of space. To reduce variance and run time, directional source-biasing was implemented. The only neutrons simulated were those that fell within the acceptable range of α on path to intercept the asteroid.

At 256,470 total spatial cells, the MCNP +F6 "collision heating" tallies stored the total energy deposited into the asteroid from all neutrons and all tracked secondary particle (photon, proton, deuteron, triton, and alpha) interactions. Secondary photons were sampled along their true paths and energy deposition was distributed accordingly. For computational savings, all charged particles were treated as local deposition because their path lengths are quite small (microns or tens of microns) compared to the size of the spatial discretization.

Some past work recognized that energy deposition from some of the capture gamma rays occurs at late times (during and/or after the material response), and opted to be more conservative in deflection calculations by entirely disregarding the depositions from secondary gamma rays [22]. In this work, capture gamma rays were included based on the recognition that the excited ^{29}Si and ^{17}O species – the predominate product nuclei formed from neutron capture in SiO_2 – are *not* metastable isomers and release their excitation energy as photons extremely quickly (in about 10^{-14} to 10^{-9} s [35]). This is within the same initial time-period that the neutrons are depositing energy, and due to this timing overlap it was assumed acceptable to include gamma ray contributions.

A key assumption in this work was that the energy deposition was instantaneous; any sense of time in MCNP was ignored, and the final tallied energy deposition profiles were simply the result of cumulative deposition. This was justified by noting that the timescales for most nuclear interactions are generally much shorter than the time required for bulk material to overcome its own inertia and physically respond. Previous work has similarly treated energy deposition via this instantaneous approximation [14,21,36,37].

4.2. Analytical approximate equation

Obtaining accurate and precise energy deposition profiles is challenging and computationally expensive. Considering the continuum of nuclear standoff distances and the wide-range of asteroid sizes, shapes, compositions, etc., energy deposition profiles for a specific problem are not always generated with full radiation transport simulations. A common method in nuclear deflection literature for quickly generating neutron energy deposition profiles is the following approximate analytical equation [19,22]:

$$E_{dep}\left(d_{NEO}, \phi\right) = E_0 \exp\left[-\frac{d_{NEO}}{\lambda_d}\right] \cos\left(\frac{\pi\phi}{2\phi_{max}}\right), \tag{5}$$

where $E_0 = \frac{\eta_Y Y_n}{4\pi s^2 \lambda_d}$ is the deposited energy density at the surface, λ_d is the characteristic length or penetration depth of the incident radiation, ϕ_{max} is the maximum irradiated surface angle (defined in Eq. (3)), η_Y is the coupling efficiency of the source energy with the asteroid, Y_n is the neutron yield, and s is the distance from the detonation to any point-of-interest on the asteroid surface. This equation assumes that energy deposition throughout the asteroid is governed by the Beer–Lambert Law of exponential attenuation. The MCNP energy deposition profiles will be compared to profiles generated by Eq. (5) in Section 5.3.

5. Neutron energy deposition

There are three pieces to this section on analyzing the neutron energy deposition results. First, the energy deposition spatial profiles from MCNP are presented and examined for 14.1 MeV and 1 MeV neutrons. Second, the energy coupling efficiencies are calculated for these two sources. Third, the MCNP profiles are compared to the analytical approximate equation from Section 4.2.

5.1. Energy deposition profiles

Figs. 5a and 5b portray, respectively, 14.1 MeV and 1 MeV energy deposition profiles, normalized per mass and per source-neutron, as functions of d_{NEO} depth across a selection of ϕ angles. The solid black horizontal lines represent the melt thresholds for 50 kt and 1 Mt detonations; regions in the asteroid located on or above these lines will be melted due to sufficiently-intense energy deposition. These melt lines will be discussed in greater detail in Section 7, along with the dashed black horizontal lines for 31.6 kt and 632 kt neutron yields.

Both figures demonstrate many similar trends. First, as the penetration depth d_{NEO} increases, the local energy deposition E_{dep} generally decreases. This is as expected. The initial incident neutron pulse is quickly attenuated via absorption and scattering reactions, and it continuously deposits fractions of its remaining energy as it travels further into the asteroid medium; this is why the energy deposition near the surface is the most intense. Second, E_{dep} decreases as the half-angle ϕ increases. The neutron fluence is at its most intense at GZ, the asteroid location closest to the standoff burst. As ϕ increases, the distance s between the detonation point-source and the asteroid surface increases, which reduces the incident neutron fluence at these more peripheral locations and therefore also reduces E_{dep}. In addition, the neutrons streaming into the curved asteroid surface are incident at a non-normal angle (with the exception of GZ), causing scatter and escape back out into space to be more likely.

Fig. 5 shows that changing the source energy can fundamentally change the spatial distribution of the deposited energy. Where d_{NEO} is less than about 25 cm, the average slopes of the E_{dep} profiles are noticeably different between Figs. 5a and 5b. A sharper (quicker) drop-off in this region is seen in the 1 MeV profiles as compared to the 14.1 MeV profiles, while the slopes appear essentially equal at deeper depths for the two sources. This trend shows that the lower-energy 1 MeV neutrons are more quickly absorbed than the more-penetrative 14.1 MeV neutrons, in agreement with the MFPs from Table 1.

An even starker spatial difference: in the 1 MeV profiles, there is a clear "plateau" in the drop-off of energy deposition in the region approximately 25 cm to 100 cm beneath the surface, and this feature is not nearly as prevalent in the 14.1 MeV profiles. This region of moderate depth is where the secondary gamma rays from the (n, γ) capture reactions deposit most of their energy. Higher-energy 14.1 MeV neutrons are more prone to be absorbed via an array of endothermic absorption reactions with ^{28}Si and ^{16}O nuclei, while lower-energy 1 MeV neutrons can exclusively react with these species via elastic scatter or exothermic (n, γ) capture. Thus, relative to the 14.1 MeV source, the 1 MeV neutrons are more frequently slowed to the types of absorptions that induce more gamma rays, which in turn travel further throughout the SiO_2 medium, forming a secondary pulse of energy deposition deeper in the asteroid. At and immediately beneath the asteroid surface, the energy deposition is predominately from direct neutron scatter and absorption reactions. In the deeper regions of the asteroid, the energy deposited is primarily from secondary gamma rays.

As confirmation, Fig. 6 shows the energy deposition profiles due to only 1 MeV neutrons (no secondaries), alongside the profiles of additional deposition from only secondary gamma rays (no neutrons). In Fig. 6a, the energy deposition profiles from neutron scattering and absorption alone – where the production of secondary gamma rays from exothermic capture reactions was disabled in this simulation – show

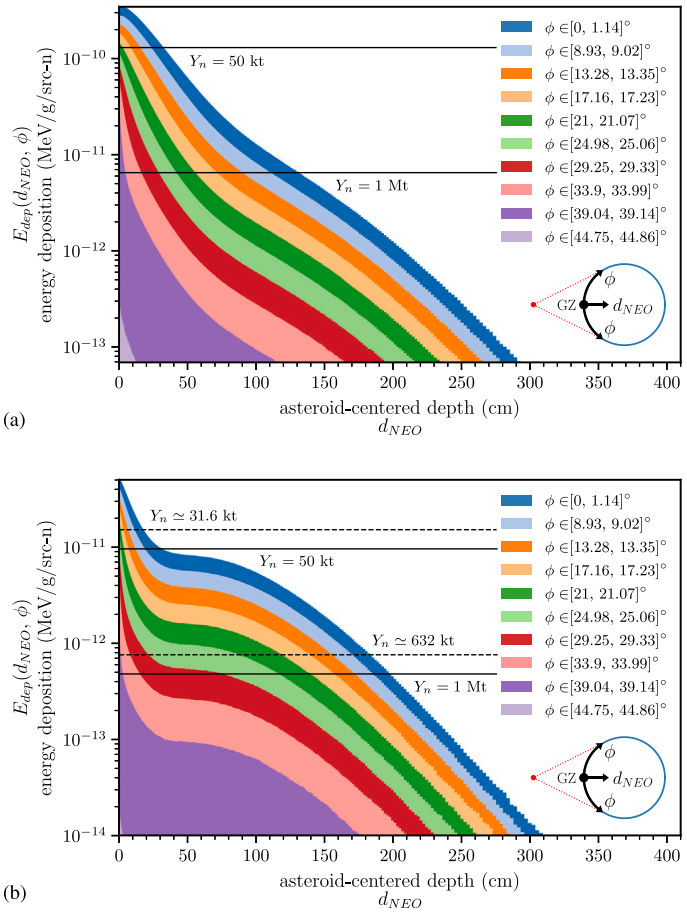

Fig. 5. Energy deposition spatial profiles for two neutron energy sources, (a) 14.1 MeV fusion neutrons and (b) 1 MeV fission neutrons. The profiles for both sources show exponential and non-exponential characteristics. The 1 MeV profiles have a distinctive "plateau" feature where the drop-off in energy deposition intensity nearly flattens over a certain region. The horizontal black lines are the melt lines, which show the depths where the melt threshold for SiO_2 is met or exceeded for select neutron yields Y_n (discussed in greater detail in Section 7). (For interpretation of the references to color in this figure legend, the reader is referred to the web version of this article.)

that most neutrons will deposit their energy at shallow depths and somewhat follow Beer's Law of exponential attenuation. The deposition from capture gamma rays alone is seen in Fig. 6b, which was created by subtracting away the neutron-only energy deposition (Fig. 6a) from the combined neutron + gamma-ray deposition (Fig. 5b). This shows that the 1 MeV plateau region is the result of the exponential neutron energy deposition profiles overlapping with the peak of the secondary gamma-ray deposition pulse. Most of these gamma rays are born after 1 MeV neutrons have lost enough energy from several scattering events in order to be thermally absorbed, which generally occurs some distance into the target. This is why the peaks of the gamma-ray depositions are for d_{NEO} values around 50–70 cm, rather than at the surface as for the incident neutrons.

At least two physical factors contribute to the asymmetries in the Fig. 6b gamma-ray profiles. First, neutron-capture-excited nuclei emit their gamma rays along directions as sampled from anisotropic angular distributions. Second, the scattered-photon differential cross section from Klein–Nishina states that Compton scatter is forward peaked with increasing gamma-ray energy, especially at the MeV-level. The geometry of the SiO_2 medium also plays a role; by chance, some of the gamma rays will escape the asteroid before depositing all of their energies, streaming outwards into space, never to return.

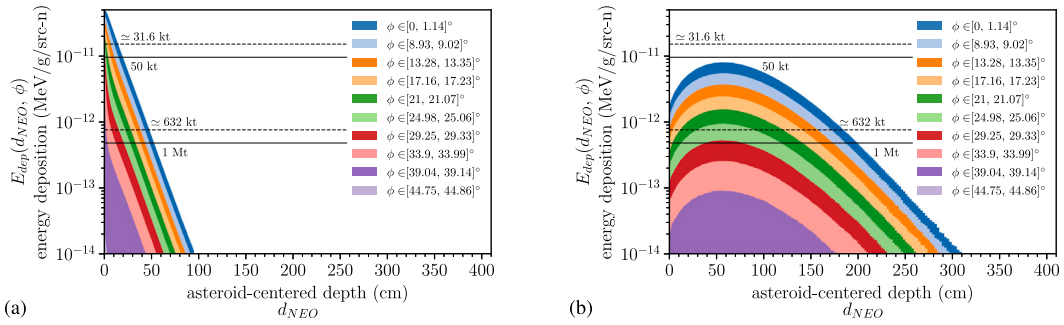

Fig. 6. Segregated energy deposition spatial profiles due to either the 1 MeV neutrons alone or their secondary gamma rays alone. (a) Resulting from the scatters and absorptions of only the 1 MeV neutrons, the primary wave of energy deposition follows a nearly exponential pattern. (b) From (n, γ) radiative capture, the isolated gamma-ray population diffuses further into the asteroid medium, forming a secondary pulse of energy deposition that is asymmetric and peaks below the surface in the asteroid interior. (For interpretation of the references to color in this figure legend, the reader is referred to the web version of this article.)

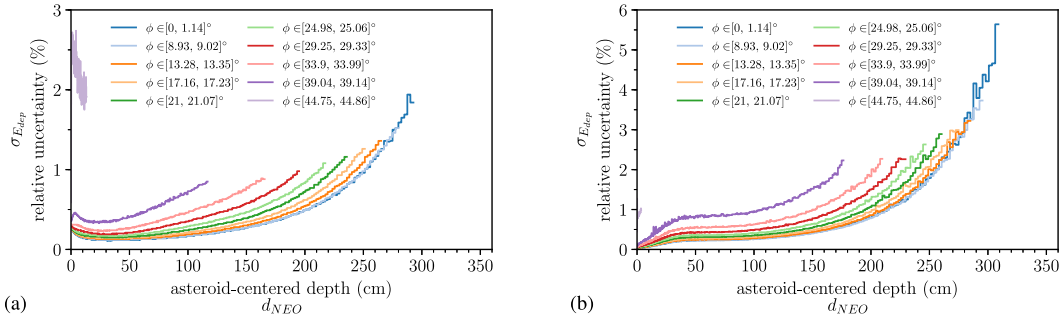

Fig. 7. Relative uncertainties in the spatial energy deposition values for the (a) 14.1 MeV and (b) 1 MeV sources. (For interpretation of the references to color in this figure legend, the reader is referred to the web version of this article.)

5.1.1. Energy tally uncertainties

For clarity in the presented results, the uncertainties in the energy deposition tallies are not shown in the Fig. 5 profiles. The statistical uncertainties were only fractions of a percent for the regions with the highest energy deposition near the surface. Fig. 7 visualizes the relative uncertainties for the energy deposition in each MCNP spatial cell for the 14.1 MeV and 1 MeV sources. The plotted uncertainties correspond to the same ranges of d_{NEO} and the same selections of ϕ that are visible in Fig. 5.

As will be shown in Section 7, the maximum melt depth considered in this work was ~200 cm. Even out to deeper ~300 cm depths, Fig. 7 shows that all spatial energy deposition values had uncertainties less than 3% for the 14.1 MeV neutrons and less than about 6% for the 1 MeV neutrons. The uncertainties out to the maximum 200 cm melt depth were generally even lower, with most tally locations quoting less than ~1% error for the 14.1 MeV neutrons and less than ~2% for the 1 MeV neutrons. The relative smoothness of the profiles in Figs. 5a and 5b allowed for these amounts of Monte Carlo uncertainties to be deemed acceptable. These levels of error were obtained by running each MCNP energy deposition simulation with five billion source neutrons.

5.2. Energy coupling efficiencies

The maximum E_{dep} magnitudes near GZ in Figs. 5a and 5b are 3.14×10^{-10} MeV/g/src-n and 4.86×10^{-11} MeV/g/src-n, respectively. The 14.1 MeV neutron source results in GZ energy deposition that is ~6.5 times greater than the deposition resulting from the 1 MeV neutrons. Of course, the lower-energy 1 MeV neutrons arrive at the asteroid surface with less energy than the 14.1 MeV neutrons, so it follows that this should result in a lower deposition intensity at GZ.

If the 1 MeV source is 14.1 times less in energy than the 14.1 MeV source, why is the difference in energy deposition instead a factor of ~6.5? This is due in part to the non-intuitive, non-linear relationship between the resulting energy deposited and the incident neutron energy. The performance factor that judges how well the incident energy is absorbed by the target is the energy coupling efficiency, which depends on the incident neutron energy, the material medium, and the source-target geometry.

As the energy of a neutron changes, so does its cross section for a given material. Lower-energy neutrons typically experience greater interaction probabilities in materials and in general have a lower MFP than the more penetrative higher-energy neutrons. Furthermore, the probabilities of endothermic interactions occurring increase with incident neutron energy. In SiO_2, 14.1 MeV neutrons have access to a myriad of reaction channels. These neutrons can interact exothermically via elastic scattering and radiative capture (n, γ); also, the 14.1 MeV source energy is greater than the thresholds for various endothermic reactions: (n,p), (n,d), (n, α), and inelastic scattering. In contrast, 1 MeV neutrons traversing SiO_2 do not meet any of these endothermic thresholds. In this medium of ^{28}Si and ^{16}O nuclei, 1 MeV neutrons only have access to elastic scattering and exothermic (n, γ) reactions. Neutrons of different energies experience different interaction mechanism probabilities and magnitudes, affecting the coupled energy.

The coupling efficiency η quantifies how much energy is deposited in comparison to all the neutron energy that actually intersects the asteroid surface, as

$$\eta = \frac{E_{dep,tot}}{Y_{int}}, \tag{6}$$

where $E_{dep,tot}$ is the total amount of energy deposited in the asteroid and Y_{int} is the intercepted yield, the amount of source radiation energy that falls within the red cone of Fig. 1a and intercepts the asteroid's surface. This quantity depends on the problem geometry; the standoff distance and the asteroid size define the half-angle α (Eq. (2)):

$$Y_{int} = Y_n \frac{\Omega_{cone}}{\Omega_{FOV}} = Y_n \frac{4\pi \sin^2 \frac{\alpha}{2}}{4\pi} = Y_n \sin^2 \frac{\alpha}{2}, \tag{7}$$

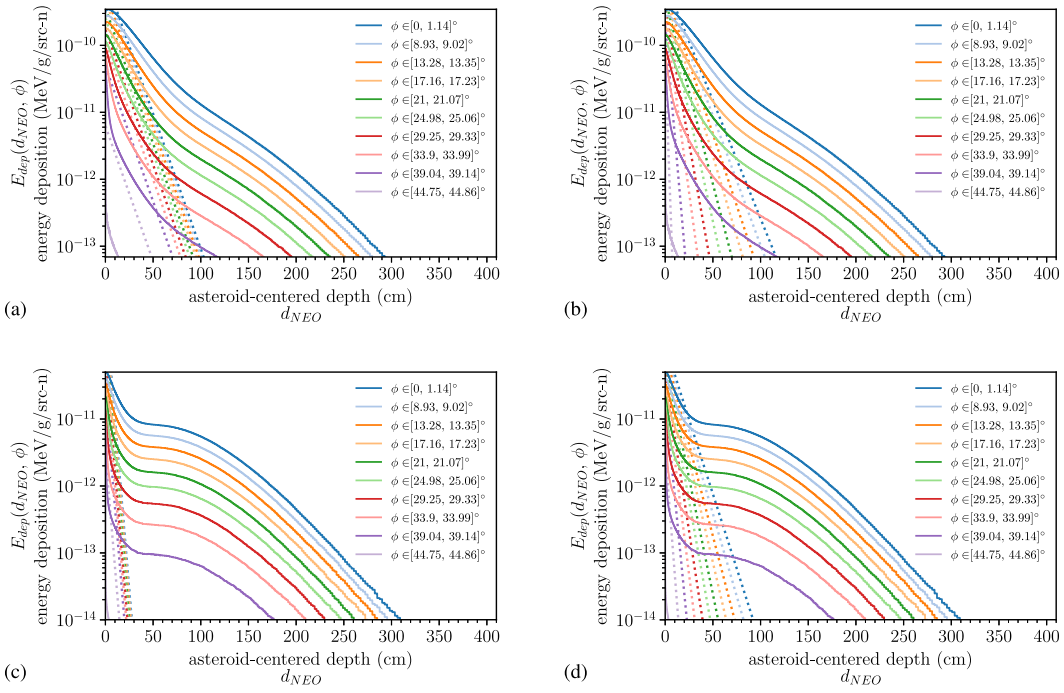

Fig. 8. Energy deposition profiles from MCNP (solid lines) and from the analytical equation (dashed lines), for 14.1 MeV neutrons (top row) and 1 MeV neutrons (bottom row), with the MFP λ_d definition (left column) and the $(1 - 1/e)\ \lambda_d$ definition (right column). (For interpretation of the references to color in this figure legend, the reader is referred to the web version of this article.)

where Ω_{cone} is the fractional solid angle of the cone of radiation that intersects the asteroid and Ω_{FOV} is the full solid angle field-of-view (4π).

Table 2 shows the coupling efficiencies for the two source neutron energies applied to the asteroid target. The coupling efficiency for the 1 MeV neutron source is greater than the 14.1 MeV source, which is in agreement with the general consensus in literature. Lower-energy 1 MeV neutrons are more readily absorbed and receive more of a "bonus" in coupling calculations due to the extra energy released from exothermic capture reactions [14]. The (n, γ) radiative capture reaction generates additional energies of 8.474 MeV or 4.143 MeV when the target nucleus is ^{28}Si or ^{16}O, respectively. Due to the kinetics of conservation of energy and momentum, most of this extra energy will initially be in the form of radiation as a secondary gamma ray (which can, in turn, soon deposit some or all of its energy into the asteroid), while the very small remaining fraction of this energy will immediately contribute to the recoil kinetic energy of the newly-formed ^{29}Si or ^{17}O nucleus. In contrast, due to their access to endothermic reaction channels, higher-energy 14.1 MeV neutrons are required to invest (or "lose") some portion of their incident source energy to initiate reactions like (n,p) or (n, α), which amounts to a coupling efficiency penalty.

The 1 MeV source has $\eta > 1$, which means that $E_{dep,tot} > Y_{int}$, or that the energy magnitude deposited into the asteroid was somehow even greater than what the initial incident neutron pulse carried. Depositing more energy than what was sent to the asteroid target is only possible because a sufficient number of the 1 MeV neutrons induced the SiO_2 system to liberate 8.474 MeV and/or 4.143 MeV of extra energies.

A widely-used notional coupling efficiency cited in literature is 0.70 for neutrons in silicate granite [13,24,38]. In comparison to the efficiencies in Table 2, this coupling fraction should be a reasonable approximation if the source is predominately high-energy 14.1 MeV neutrons as from a fusion device, but it underestimates the η values resulting from 1 MeV neutrons, as would be seen in a fission spectrum.

5.3. Comparison to analytical equation

The MCNP energy deposition profiles can be compared to profiles generated by the analytical approximate method from Section 4.2.

Table 2
Energy coupling efficiencies for two neutron energies.

E_n	η
14.1 MeV	0.6884
1 MeV	1.0896

There are two ways to use Eq. (5) based on two possible definitions of λ_d, the characteristic path-length parameter. The primary definition is that λ_d is the MFP of the source neutrons in the given asteroid medium [22]. The values in Table 1 were used for this interpretation of Eq. (5).

A second way to define λ_d allows for an alternate usage of Eq. (5). Now, λ_d is redefined to be the penetration depth at which a fraction $(1 - 1/e)$ of the total energy has been deposited [14]. This definition means that radiation transport simulation results are required to calculate λ_d. A $(1 - 1/e)\ \lambda_d$ was calculated for each angular bin from the MCNP outputs. The total energy deposited in each conical region was calculated, and linear interpolation determined the depth where the $(1 - 1/e)$ fraction of this total energy was reached.

Note that, as written, E_0 in Eq. (5) is volumetric with units of MeV/cm^3. To directly compare Eq. (5) profile magnitudes to their per-mass-normalized MCNP counterparts, the formula was divided by the bulk SiO_2 density of 1.855 g/cm^3. The coupling efficiencies η_Y were taken as the η values from Table 2. Because the MCNP energy deposition is normalized as per source neutron (MeV/g/src-n), the yield Y_n within E_0 in Eq. (5) was simply E_n, the energy of one source neutron (i.e. MeV/src-n). The Eq. (5) profiles were angularly discretized in the same way that the MCNP results were, allowing for direct comparison. A linearly-spaced survey of ϕ was sampled, allowing for an *average* surface energy deposition E_0 along with an *average* cosine term in Eq. (5) to be calculated for each conical region.

Figs. 8a and 8c show the MCNP profiles alongside the analytical equation profiles using the MFP definition of λ_d for 14.1 MeV and 1 MeV source neutrons, respectively. Figs. 8b and 8d visualize the profile comparison for the $(1 - 1/e)\ \lambda_d$. The dashed lines are the Eq. (5)

analytical profiles, and the solid lines are the MCNP simulated profiles. Both the analytical profiles and the MCNP profiles are color-coded according to the ϕ legend.

In general, the MFP λ_d overestimates the energy deposition at the surface for most angles for both source energies (more strongly so for 1 MeV than 14.1 MeV). The MFP method also performs poorly as d_{NEO} increases, with the Eq. (5) energy deposition clearly and quickly diverging from the MCNP-calculated energy deposition. Note that the energy deposition due to neutrons only – for example, the 1 MeV neutrons alone in Fig. 6a – is much closer to the pure exponential shape that Eq. (5) requires.

The $(1 - 1/e)\ \lambda_d$ in the analytical equation also results in overestimates for surface depositions from both sources. Relative to the MFP definition, this application of Eq. (5) appears to generate profiles in closer agreement with the MCNP profiles, although there is still great divergence. Non-exponential energy deposition patterns are clearly visible in the MCNP results, especially the distinct plateau region in the 1 MeV profiles, which strongly deviates from exponential attenuation.

This analytical formula relies on the simplifying assumption (or rather, approximation) that energy deposition decays purely exponentially with the path-length, and neither path-length definition for λ_d truly describes the nature of the energy-dependent profiles. Because of this, in terms of how the energy is spatially distributed throughout the asteroid, the Eq. (5) profiles show significant departure from the MCNP profiles. While it is convenient to express energy deposition as an expedient formula, in reality neutron scatter and capture reactions and angular anisotropies generate more complex energy deposition profiles. The energy deposition spatial features from the high-fidelity MCNP results are critical inputs to the subsequent hydrodynamic simulations investigating the deflection impact of the neutron source energy.

6. ALE3D methodology

To determine the effects from the differing spatial profiles and energy coupling efficiencies, the MCNP energy deposition outputs served as input conditions to a hydrodynamic asteroid model in ALE3D. The resulting asteroid velocity change, δV, was the metric used to compare deflection performance.

6.1. Asteroid model

The simulated asteroid in ALE3D, like its MCNP counterpart, was monolithic, 300 m in diameter, non-rotating, and composed of SiO_2. The material model for SiO_2 used in this work belongs to the GEODYN library and references Livermore Equation of State (LEOS) #2210 for silicon dioxide.[2] LEOS #2210 is SiO_2 at a standard solid density of 2.65 g/cm^3. The microporosity Φ was set to 0.30 (30%), making the bulk or effective material density of the asteroid 1.855 g/cm^3. In this way, the ALE3D material composition and density matched the MCNP simulations.

The material model makes use of the geologic constitutive Cap model to contribute strength characteristics to the SiO_2 material, making the asteroid a rigid or cohesive body rather than rubble. Also, LEOS #2210 prescribes SiO_2 at a reference temperature of 290.1112 K, although typical asteroids are believed to have average temperatures around 100–200 K [39]. This small difference in initial temperature conditions was considered negligible in comparison to the temperature increases of thousands of Kelvin, or even tens of thousands of Kelvin, seen from the neutron energy deposition.

Unlike MCNP, which requires 3-D surfaces, ALE3D was able to model the asteroid as a 2-D semi-circle via axisymmetric geometry (i.e. as Fig. 4a). This is done to save computational time and memory, while also allowing for finer spatial mesh resolution for a given number of elements or zones; this geometric approach has been used in past work [13]. The Wilkins method for 2-D axisymmetric configurations was selected [31].

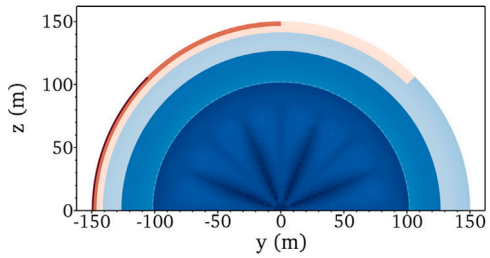

Fig. 9. Illustration of the ALE3D asteroid mesh resolution. The thin, darkest red strip is where the mesh is most refined: on the left irradiated face, at the outer surface, between GZ (ϕ = 0°) and 45° off from GZ. This is the sensible energy deposition region, where zones are ~1-to-2.5 cm squares. Cooler and cooler colors show that the mesh resolution is gradually coarsened. The zonal sizes increase both as ϕ increases along the surface curvature and as d_{NEO} increases in depth, at the locations moving away from the energy deposition region. (For interpretation of the references to color in this figure legend, the reader is referred to the web version of this article.)

A given asteroid mesh in ALE3D had between 419,136 and 747,200 total zonal elements; a custom mesh discretization was created for each neutron energy + neutron yield configuration. The mesh resolution was not uniform throughout the entire asteroid model. Using several ALE3D capabilities – including non-linear transforms, mesh rotations, merge operations, slide surfaces, and transition elements [31] – the full semi-circle mesh was the union of four sub-mesh quadrants, each 45° in extent, each with different zonal discretizations. This complex mesh structure allowed for sufficient resolution to be achieved in the small, thin, localized region of interest – the irradiated surface where melted blow-off originates – without the unwieldy expense of maintaining such refinement throughout the entire 300 m object. Fig. 9 maps the mesh resolution by color to visualize the discretization approach in ALE3D. The colorscale is logarithmic, with colors in the red–orange spectrum representing high resolution and deeper blues highlighting low resolution. The very thin strip of dark red on the left face of the asteroid identifies the 45° energy deposition region of the mesh, where the zones are ~1-to-2.5 cm squares. On the opposite end of the spectrum, the dark blue covers the area where the zones on the order of 250 cm per side. In the various ALE3D configurations, the dark red strip contained between 34.9% and 64.5% of all the zones in the entire asteroid mesh.

6.2. Energy deposition

ALE3D circular meshes reference an (r, θ) coordinate system, where r = 150 m is the outer asteroid surface and θ = 0° is on the positive y-axis between mathematical quadrants I and IV. However, it was more convenient to process the energy deposition tallied in MCNP as (d_{NEO}, ϕ), with d_{NEO} = 0 m representing the surface and ϕ = 0° located at GZ on the negative y-axis between quadrants II and III. With a mapping of these two coordinate systems required, the import process was achieved using 1-D and 2-D tables, space tables, and the heatgen function for heat generation throughout space in ALE3D [31]. It was neither possible nor desirable for ALE3D's mesh structure to exactly match the MCNP cell resolution. Because of this, the MCNP data was logarithmically interpolated to assign an appropriate energy deposition to each ALE3D zone based on its (d_{NEO}, ϕ) spatial location.

Heatgen defines a rate-based generation of energy over time. To achieve "instantaneous" energy deposition in ALE3D, heatgen was only active for the first computational cycle, which was prescribed the initial time-step of $\Delta t_0 = 1{\times}10^{-5}$ μs. The desired neutron yields were simulated by scaling the normalized MCNP profiles (in units of MeV/g/src-n; see Fig. 5) by the corresponding number of source neutrons.

[2] This material model was developed by Eric Herbold of LLNL's Computational Geosciences Group.

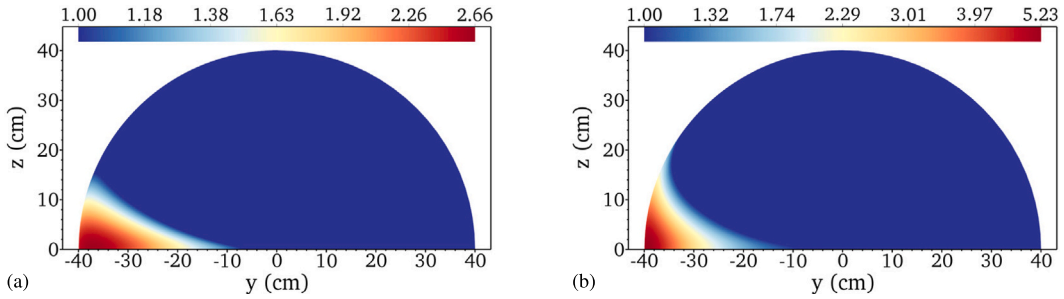

Fig. 10. Asteroidal energy deposition heatmaps generated from a standoff 50 kt neutron yield, visualized on a small 0.8 m asteroid. Areas with colors other than dark blue are melted. (a) The 14.1 MeV neutrons heat parts of the asteroid to 2.66 times above the melt threshold for SiO_2, while (b) the 1 MeV neutrons push to 5.23 times beyond the melt minimum. With GZ located here at coordinates $(-40, 0)$ cm, the maximum melt depth for the 14.1 MeV neutrons is about 33 cm beneath GZ and ~31 cm for the 1 MeV source. (For interpretation of the references to color in this figure legend, the reader is referred to the web version of this article.)

6.3. Blow-off response

The resulting deflections in the x and z directions are zero due to symmetry (see Fig. 1). Tracking the time-dependent y-momentum and mass of either the blow-off (which will be oriented in the −y direction) or the asteroid (which will be in the +y direction) can determine δV; this work opted for the latter option. From the moment immediately following the energy deposition, the conservation of momentum determines the change in asteroid velocity, δV, to be

$$\delta V = \frac{\sum_i m_{asteroid,i} v_{asteroid,i}}{M_{asteroid}}, \tag{8}$$

where $m_{asteroid,i}$ and $v_{asteroid,i}$ are respectively the i^{th} time-evolving asteroid zonal mass and y-velocity, and $M_{asteroid} = \sum_i m_{asteroid,i}$. The masses and velocities of the blow-off were *not* counted in these sums by masking against zones that were both (1) melted according to the LEOS for SiO_2 in the material model, and (2) traveling at speeds greater than the escape velocity for the 300 m asteroid.

Note that the escape velocity threshold is directional. A coordinate transform for each individual zone was required: zonal velocities v_y and v_z in the y and z directions were converted to the effective velocity $v_\perp$, which is the speed of each zone in the outward direction with respect to the asteroid's center-of-mass:

$$v_\perp = -v_y \cos\phi + v_z \sin\phi. \tag{9}$$

Melted material in a zone is only counted as blow-off if its $v_\perp$ is greater than the surface escape velocity, which is 15.27 cm/s for the asteroid in this study. This escape velocity condition for the blow-off was how gravitational forces were incorporated; the ALE3D simulations did not include a direct model for gravity.

The prompt momentum impulse from melted blow-off finishes evolving only a few hundred microseconds after the energy deposition from a standoff nuclear detonation [40]. In these short timescales, negligible heat transfer occurs. Thus, asteroid response simulations in ALE3D are run "hydro-only," with thermal transport turned off, simplifying the problem and saving computational time; there is precedence for this in past work [41].

6.4. Error in blow-off momentum

The selected zonal sizes in the ALE3D simulations were not arbitrary. They were chosen by consulting an empirical formula from past work that correlates the error in blow-off momentum with the hydrodynamic mesh resolution [14]:

$$\%\ \text{Error} \approx 24 \frac{\Delta r}{z_{melt}}, \tag{10}$$

where Δr is the zone size and z_{melt} is the melt depth for the energy deposition profile, which is the maximum distance beneath the surface where the melt threshold of the material is reached. The melt threshold for SiO_2 is approximately 1941 J/g [42].

The maximum melt depth in the scenarios of this paper ranged from 19 cm up to ~200 cm. This is seen by the intersection of the horizontal black melt lines in Fig. 5 with the dark blue $\phi \in [0, 1.14]°$ profiles that encompass GZ. With these z_{melt} values, by Eq. (10), square zones with a Δr between ~1 cm and 2.5 cm per side in the asteroid's irradiated surface region were small enough to achieve between 0.27% and 1.33% error in the blow-off momenta.

7. Asteroid deflective response

There are four components to this section analyzing the results for asteroid deflective response. Sections 7.1 and 7.2 compare the deflection performance – via the asteroid velocity change δV – between 14.1 MeV and 1 MeV neutron energies with equivalent 50 kt and 1 Mt neutron yields. Sections 7.3 and 7.4 take a different approach, comparing equivalent ~5 kt and ~100 kt neutron energy depositions.

7.1. 50 kt neutron yields

Fig. 10 shows the 14.1 MeV and 1 MeV heatmaps of asteroidal energy deposition, as resulting from a 50 kt neutron yield at a $c \approx 0.414$ standoff distance. The colorbars are logarithmically scaled, plotting the dimensionless quantity E_{dep}/E_{melt}, where E_{dep} is the energy deposition at a given location in J/g and E_{melt} is the 1941 J/g melt threshold for SiO_2.

Note that the 2-D energy deposition profiles from Fig. 5 have been mapped on to a very-small 0.8 m diameter asteroid in Fig. 10, rather than the full 300 m target in this work. This artificially enlarges the area of the energy deposition region in order to better visualize the heating gradients. The $\phi = 0°$ to $\phi = 45°$ arc-length of the irradiated surface area of the 300 m asteroid is nearly 11,800 cm, but the z_{melt} melt depths from the 50 kt neutron yields are only ~33 cm and ~31 cm for 14.1 MeV and 1 MeV neutrons, respectively. It is bothersome that the irradiated region is very long in ϕ and very shallow in d_{NEO} on the 300 m body (the thin, darkest red strip in Fig. 9). Viewing the profiles on a much smaller object, however, allows the deposition depth to be visible along with the curvature of the surface.

The 1 MeV neutrons clearly melt a greater fraction of the 45° irradiated surface area, in agreement with the $Y_n = 50$ kt melt lines in Fig. 5. The 50 kt melt line for 14.1 MeV neutrons extends out to approximately $\phi \in [21, 21.07]°$ (the dark green profile in Fig. 5a), while for 1 MeV neutrons the melt line touches all the way out to $\phi \in [33.9, 33.99]°$ (the light red profile in Fig. 5b).

With $\alpha = 45°$, Eq. (7) reveals that Y_{int}/Y_n is ~0.1464. For the 50 kt standoff neutron yield, approximately 7.32 kt is intercepted by the asteroid target. However, due to the differences in the energy coupling efficiencies (see Table 2) and in the finite mesh structures in ALE3D, the 14.1 MeV source deposited 5.04 kt in the object, while the 1 MeV neutrons deposited 7.96 kt in total.

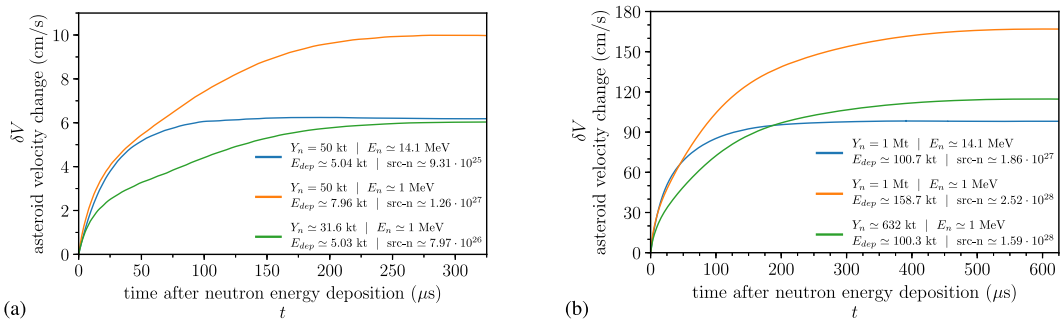

Fig. 11. Summary of asteroid responses to various neutron yields, energy depositions, and source neutron energies. The change in asteroid velocity over time is compared, as resulting from either (a) 50 kt neutron yields and/or 5 kt energy depositions, or (b) 1 Mt neutron yields and/or 100 kt energy depositions. The bands of lighter blue/orange/green indicate the 1-σ uncertainty in the δV values due to the ALE3D mesh resolution (Eq. (10)). Not all uncertainty bands are visible on this scale. (For interpretation of the references to color in this figure legend, the reader is referred to the web version of this article.)

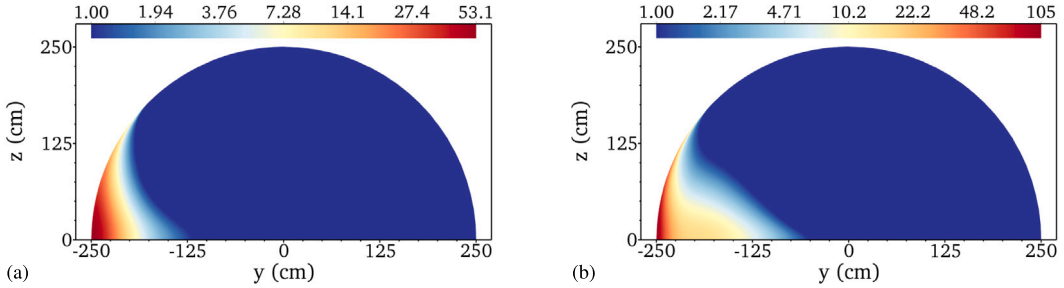

Fig. 12. Asteroidal energy deposition heatmaps generated from a standoff 1 Mt neutron yield, visualized on a small 5 m asteroid. Dark blue paints the regions where the asteroid remains solid. (a) The 14.1 MeV neutrons induce a peak heating intensity of 53.1 times the SiO_2 melt threshold, while (b) the 1 MeV neutrons heat some of the asteroid material to 105 times past the melt minimum. Beneath GZ, located here at $(-250, 0)$ cm, the maximum melt depths amount to ~130 cm with 14.1 MeV neutrons and slightly less than 200 cm with 1 MeV neutrons. (For interpretation of the references to color in this figure legend, the reader is referred to the web version of this article.)

Both asteroid response simulations in ALE3D were run for several hundred microseconds. For the 50 kt yield, for both 14.1 MeV and 1 MeV sources, the rapid momentum impulse due to the blow-off reached a steady value ~300 μs after the neutron energy deposition. Shown in Fig. 11a, the δV at 300 μs is 6.19 ± 0.06 cm/s for the 14.1 MeV neutrons (blue line) and 9.99 ± 0.12 cm/s for the 1 MeV neutrons (orange line). This means that the 1 MeV neutrons offer about 1.61 ± 0.02 times better deflection performance than 14.1 MeV neutrons at equivalent 50 kt detonation yields.

Because the 1 MeV neutrons have a much higher coupling efficiency, 58% more total energy was deposited in the asteroid compared to the 14.1 MeV neutrons. This simple difference in deposition magnitude due to coupling efficiency might account for most of the ~61% difference in δV values. It is also possible that the distinct spatial qualities of the energy deposition profiles (Fig. 10) are influencing the resulting deflections. Decoupling the relative effects of each energy deposition facet (green lines in Fig. 11) will be explored in Sections 7.3 and 7.4.

7.2. 1 Mt neutron yields

The neutron yield was increased by a factor of twenty, from 50 kt to 1 Mt. Fig. 12 contrasts the energy deposition heatmaps of the 14.1 MeV and 1 MeV neutrons at 1 Mt yields, visualized on a small 5 m asteroid. The peak E_{dep}/E_{melt} values have increased by a factor of twenty compared to Fig. 10, but the z_{melt} melt depths have not. For the 1 Mt yield, z_{melt} is about 130 cm and 200 cm for 14.1 MeV and 1 MeV neutrons, respectively. The melt depths do not scale linearly with the yield because the energy deposition profiles in Fig. 5 are not linear. Also, at this larger yield, 14.1 MeV and 1 MeV neutrons equally melt ~44.96° of the 45° irradiated surface extent.

About 100.7 kt of the 14.1 MeV source is deposited in the ALE3D asteroid, and the 1 MeV neutrons deposit ~158.8 kt. The time necessary for the blow-off momentum to reach a steady value was increased to 600 μs because of these larger energy depositions. The δV at 600 μs, shown in Fig. 11b, is 98.09 ± 0.41 cm/s for the 14.1 MeV neutrons (blue line) and 166.9 ± 0.5 cm/s for the 1 MeV neutrons (orange line). Thus, 1 MeV neutrons offer about 1.70 ± 0.01 times better deflection performance than 14.1 MeV neutrons at equivalent 1 Mt detonation yields.

As the δV of an asteroid approaches its escape velocity v_{esc}, fragmentation becomes difficult to avoid [13]. Currently, the planetary defense community often assumes that a δV of ~10% or more of the asteroid's escape velocity is an approximate threshold for accidental weak disruption [43]. For the asteroid in this work – a spherical object with a diameter of 300 m and a bulk density of 1.855 g/cm^3 – the mass of the body is 6.216×10^{16} g, and the surface escape velocity v_{esc} is 15.27 cm/s.

The δV resulting from a 1 Mt yield of either neutron source energy far exceeds the escape velocity, and therefore 1 Mt is easily too large for deflecting this asteroid. Even the 50 kt δV values in Section 7.1 exceed the $1/10^{\text{th}}$ v_{esc} risk threshold. To safely deflect this Apophis-sized asteroid, intact, at this $c \approx 0.414$ standoff distance, a slightly lower yield would likely be preferable, which is in agreement with past work [13]. Regardless, for the central purpose of this study – to investigate the effects of the neutron energy on deflection – these asteroid response data are still useful for comparison.

The planetary defense community also generally believes that imparting a δV of at least ten times an asteroid's surface escape velocity is sufficient to "robustly" *disrupt* the object. In this disruption regime, the asteroid is wholly broken into many small pieces. Assuming a reasonable lead time, these pieces are so widely scattered that very few, if any, are likely to stay on-path to reach the Earth–Moon system. Even if the largest asteroid fragments could somehow stay the course and still collide with Earth, these would be small enough to burn up harmlessly in the Earth's atmosphere. Not only is the ~166.9 cm/s

velocity change from the 1 Mt burst of 1 MeV neutrons far too extreme for deflection, but under the "robust" disruption heuristic of $10 \times v_{esc}$, this δV is sufficient for the asteroid to be considered entirely shattered.

At 1 Mt, the 1 MeV source outperformed the 14.1 MeV source, similar to the 50 kt case in Section 7.1. The same observations of energy coupling efficiency and energy deposition profiles still apply. However, there is one difference of note: the relative δV ratio between the two neutron energies was 1.61 ± 0.02 at 50 kt, but it was 1.70 ± 0.01 at 1 Mt. The only features of energy deposition that did not proportionately scale with respect to the yield were the angular extent and melt depth, due to the spatial profile differences. Compared to 14.1 MeV neutrons, it appears that 1 MeV neutrons offer energy deposition profiles that are more advantageous for deflection, and this effect is more significant at larger yields.

7.3. 5 kt energy depositions

Sections 7.1 and 7.2 compared the deflection performance for equal yields. As in Table 2, η is 1.0896 for 1 MeV neutrons and 0.6884 for 14.1 MeV neutrons – a ratio of 1.58 between the two couplings. At equal yields, the 1 MeV neutron source will always deposit 58% more total energy in the asteroid. In order to remove the energy coupling efficiency advantage and study only the spatial distribution effects, the neutron yields for the 1 MeV source are now reduced by this factor of 1.58. This equalizes the energy deposition magnitudes for the two neutron sources. In this subsection, the deflection outcome from a 50 kt yield of 14.1 MeV neutrons is compared to ~31.6 kt of 1 MeV neutrons (each depositing ~5 kt of total energy). In Section 7.4, 1 Mt of 14.1 MeV neutrons is compared to ~632 kt of 1 MeV neutrons (each depositing ~100 kt of total energy). Any difference in δV is now the result of the energy deposition spatial profiles, alone.

Shown by the 31.6 kt melt line in Fig. 5b, this reduced yield of 1 MeV neutrons results in a maximum melt depth of 19 cm, lower than the 31 cm mark reached by the 50 kt yield in Section 7.1. The 14.1 MeV neutrons deposit approximately 5.04 kt in the asteroid, and 1 MeV neutrons deposit 5.03 kt. This <0.08% difference is due to the finite ALE3D mesh structures. Fig. 11a shows that the asymptotic δV at 300 μs is 6.19 ± 0.06 cm/s for the 14.1 MeV neutrons (blue line) and 6.02 ± 0.08 cm/s for the 1 MeV neutrons (green line). The 14.1 MeV neutrons are 1.03 ± 0.02 times more effective than 1 MeV neutrons at equivalent ~5 kt depositions.

At this level of energy deposition, there is not a discernible difference in deflection performance between 14.1 MeV and 1 MeV neutrons. The 3% increase in δV for 14.1 MeV neutrons over 1 MeV neutrons in quite small, given that the error bound on this factor is ±2%, along with the 0.08% unfair advantage in energy deposition magnitude for the 14.1 MeV ALE3D asteroid. It is worth noting that the 31.6 kt yield of 1 MeV neutrons is *not* enough to melt the plateau region (see Fig. 5b). Considering the 50 kt melt line for the 14.1 MeV neutrons and the 31.6 kt melt line for the 1 MeV neutrons in Fig. 5, the extents and relative intensities of the two melted regions are not too different. This can explain why there is almost no difference in the resulting δV speeds. With the findings from this subsection and Section 7.1, the magnitude of energy deposition – determined by the neutron yield and the energy coupling efficiency – has a stronger effect on δV than the energy's spatial distribution.

7.4. 100 kt energy depositions

The 5 kt energy depositions were increased by twenty, requiring a 1 Mt yield of 14.1 MeV neutrons and a ~632 kt yield of 1 MeV neutrons. The 14.1 MeV neutrons deposited ~100.7 kt in the asteroid, and 1 MeV neutrons deposited 100.3 kt, a small relative difference of <0.4%, again resulting from the ALE3D mesh structures. The z_{melt} for the 14.1 MeV source remained at 130 cm, but for 1 MeV neutrons it slightly decreased from 200 cm to about 180 cm. This difference is evident from the 1 Mt and 632 kt melt lines in Fig. 5b. In Fig. 11b, the δV at 600 μs is 98.09 ± 0.41 cm/s for the 14.1 MeV neutrons (blue line) and 114.7 ± 0.34 cm/s for the 1 MeV neutrons (green line). For 100 kt of deposition, 1 MeV neutrons enable a velocity change that is 1.17 ± 0.01 times greater than 14.1 MeV neutrons.

The energy deposition profiles have a greater influence on asteroid deflection at higher yields due to the plateau region that is only present in the 1 MeV energy deposition profiles. Resulting from a 632 kt yield of 1 MeV neutrons, the 100 kt deposition pushes into the target and melts many of the asteroid locations that fall within the plateau region, as shown by the 632 kt melt line in Fig. 5b. With a sufficiently-high yield, reaching this 1 MeV plateau region allows for greater and more energetic amounts of blow-off. Note in Fig. 12 that the areal extents and peak intensities of the 1 MeV melted materials are quite greater than their 14.1 MeV counterparts. As a result, at equal 100 kt energy depositions, the competing 14.1 MeV and 1 MeV neutrons achieve deflection performances that differ by 17% in favor of the latter.

8. Conclusions

In order to correctly predict an asteroid's deflective response to a nuclear device detonation, it is important to accurately quantify the neutron energy deposition and, in turn, the resulting change in the asteroid's velocity. The effects of 14.1 MeV and 1 MeV source neutron energies were explored for 50 kt and 1 Mt neutron yields and for 5 kt and 100 kt energy depositions. For each case, the resulting blow-off momentum impulse determined the asteroid velocity change, δV.

A 300 m SiO_2 asteroid was modeled in MCNP, and the neutron energy deposition was calculated from a nuclear device detonation at a standoff distance of ~62.13 m. A custom methodology was developed to efficiently discretize the energy deposition spatial tallies in angle and in depth. With the high-fidelity MCNP simulations, it was shown that both the energy deposition profiles and the energy coupling efficiencies are distinct between 14.1 MeV and 1 MeV neutron sources. Most of these differences are the result of the different types of secondary particles that the SiO_2 medium is induced to release. 14.1 MeV neutrons tend to produce charged particles through endothermic reactions with SiO_2; 1 MeV neutrons have cross sections that only allow for exothermic reactions that create more gamma rays. 1 MeV neutrons induce a flattened "plateau" region in their energy deposition profiles due to the gamma rays released in radiative capture; 14.1 MeV profiles lack this spatial feature due to reaction channel differences. The 14.1 MeV fusion neutrons have a coupling efficiency close to 0.70, in agreement with couplings used in past literature; however, 1 MeV fission neutrons achieve a coupling efficiency of ~109% if their secondary gamma rays are included. Additionally, it was shown that analytical exponential profiles are a poor approximation of the complex spatial patterns of energy deposition that are created by neutron scatter and capture reactions. Consequently, there should be greater confidence in the deflection outputs when more-accurate energy deposition profiles – as can be obtained from MCNP or other radiation transport simulations – are used as inputs.

The asteroid deflective responses to the two neutron sources were simulated using ALE3D. There were several comparative scenarios with varying neutron yields and energy depositions, as summarized in Table 3. Differences in the energy deposition profiles alone had a negligible effect on deflection at equal 5 kt depositions with relatively-shallow melt depths; however, for more-penetrating 100 kt depositions, 1 MeV neutrons were able to melt their profile's plateau region, which greatly expanded the blow-off volume and induced a 17% greater δV than 14.1 MeV neutrons. When both the energy deposition profiles *and* the energy coupling efficiencies are factors – that is, for equal neutron yields – 1 MeV neutrons offered a 61% better performance at 50 kt yields and a 70% improvement at 1 Mt yields. While the variations in the spatial profiles do have some impact, these effects are yield-dependent, and the magnitude of energy deposition – determined by

Table 3
Summary of asteroid velocity changes δV due to total energy depositions $E_{dep,tot}$, which in turn result from two source neutron energies E_n and various standoff neutron yields Y_n.

Y_n	E_n	$E_{dep,tot}$	δV
50 kt	14.1 MeV	5.036 kt	6.19 ± 0.06 cm/s
50 kt	1 MeV	7.979 kt	9.99 ± 0.12 cm/s
31.59 kt	1 MeV	5.041 kt	6.02 ± 0.08 cm/s
1 Mt	14.1 MeV	100.68 kt	98.09 ± 0.41 cm/s
1 Mt	1 MeV	158.75 kt	166.9 ± 0.50 cm/s
631.8 kt	1 MeV	100.30 kt	114.7 ± 0.34 cm/s

the yield and the source's energy coupling efficiency – appears to be the most important determinant of the resulting δV.

To deflect this work's 300 m asteroid while minimizing the risk of accidental weak disruption, smaller velocity changes – especially perturbations below 10% of the object's 15.27 cm/s escape velocity – from ~62 m standoff yields lower than 50 kt would be preferred.[3] At this lower regime of energy deposition, as would also be applied to even smaller targets, it is unlikely that changing the energy deposition profile would have a significant impact on deflection. Conversely, if a larger asteroid is to be deflected by a larger yield at standoff, then the spatial differences in the energy deposition could play a more important role and should be accounted for when determining the total asteroid deflection in a given scenario. While the energy deposition profile is only sometimes a strong factor, the energy-dependent coupling efficiency is *always* important to consider, as it can result in dramatic changes in the total energy deposited.

In the future, some of the key assumptions of this work should be revisited and improved upon, especially the idea that the radiation and hydrodynamic timescales are so well separated for neutron interactions that loosely coupled simulations are permissible and "instantaneous" energy deposition is valid. This might not be the case for the secondary gamma-ray deposition, or even the final stages of the neutron deposition. It could be necessary to tally the radiation energy deposition both spatially and temporally, which would add complexity and also require a new set of assumptions and justifications in the MCNP-ALE3D coupling; other codes that combine radiation and hydrodynamics in one unified package might be more appropriate for this type of asteroid deflection simulation.

Furthermore, larger parametric studies of neutron yields, standoff distances, neutron energies, and asteroid targets might unveil new discoveries. In particular, perhaps the deflection performance from 2.45 MeV deuterium–deuterium fusion neutrons could be studied. Better still, more realistic outputs from nuclear devices should be considered. Neutrons from an explosion are emitted across an energy spectrum; as a source, this would be more accurate than the simplified, approximately-monoenergetic 14.1 MeV and 1 MeV neutrons used in this work. To determine the total asteroid deflection, incorporating the depositions from the prompt x-rays and gamma rays with the neutrons could also be of interest.

The results of this paper can be used to inform future simulations for determining the optimal source neutron energy spectrum for asteroid deflection applications.

[3] The safe-for-deflection yield from a nuclear device could be calculated for a fixed standoff distance and known asteroid properties. Alternatively, for a standoff nuclear device with a given yield that would induce a δV that is too intense for deflection, it is probably more practical to retain the same device and merely increase the standoff distance, thereby lessening the amount of energy deposited. The fact that the induced δV is tunable by simply changing the standoff distance mid-mission is another advantage of nuclear devices for asteroid deflection/disruption. The ability to quickly and dynamically increase or decrease the standoff distance could be especially helpful if additional details on the asteroid size, structure, geometry, and/or composition are only determined after the interceptor spacecraft has already been launched with a device of a known yield.

Declaration of competing interest

The authors declare that they have no known competing financial interests or personal relationships that could have appeared to influence the work reported in this paper.

Acknowledgments

This work was performed under the auspices of the U.S. Department of Energy by Lawrence Livermore National Laboratory under Contract DE-AC52-07NA27344. LLNL release number: LLNL-JRNL-814393. We further acknowledge that this research was supported by the National Nuclear Security Administration under grant NA000103 and by the SMART Scholarship-for-Service program.

The authors would like to thank Dr. John McClory and Lt Col Michael Dexter for feedback during the process of this research. Additionally, we thank the developers of ALE3D, especially Andy Anderson, Albert Nichols III, and Chad Noble, for their extended technical support. Lastly, thanks are given to Eric Herbold of LLNL's Computational Geosciences Group for his help with his GEODYN SiO_2 material model.

The views expressed in this article are those of the authors and do not necessarily reflect the official policy or position of the United States Air Force, the Department of Defense, the Department of Energy, or the United States Government.

References

[1] L.S. Horan IV, D.E. Holland, M. Bruck Syal, J. Wasem, M.L. Dexter, J.E. Bevins, Neutron Energy Effects on Asteroid Deflection, in: 2020 IEEE Aerospace Conference, 2020, http://dx.doi.org/10.1109/AERO47225.2020.9172255.

[2] National Near-Earth Object Preparedness Strategy and Action Plan, Office of Science and Technology Policy, 2018, URL https://www.whitehouse.gov/wp-content/uploads/2018/06/National-Near-Earth-Object-Preparedness-Strategy-and-Action-Plan-23-pages-1MB.pdf.

[3] I. de Pater, J.J. Lissauer, Planetary Sciences, Cambridge University Press, 2015.

[4] S.D. Pippo, Near-Earth Objects and Planetary Defence, United Nations Office for Outer Space Affairs, 2018, URL https://www.unoosa.org/documents/pdf/smpag/st_space_073E.pdf.

[5] P. Chodas, Discovery Statistics, NASA JPL Center for Near Earth Object Studies, 2019, URL https://cneos.jpl.nasa.gov/stats/totals.html.

[6] P. Tricarico, The near-Earth asteroid population from two decades of observations, Elsevier Icarus (2016) http://dx.doi.org/10.1016/j.icarus.2016.12.008.

[7] B. Betts, Will an Asteroid Hit Earth? Your Questions Answered., Planet. Soc. (2018) URL https://www.planetary.org/blogs/bruce-betts/will-an-asteroid-hit-earth.html.

[8] Effects of Nuclear Weapon Testing by the Soviet Union, Comprehensive Nuclear-Test-Ban Treaty Organization, 2019, URL https://www.ctbto.org/nuclear-testing/the-effects-of-nuclear-testing/the-soviet-unionsnuclear-testing-programme/page-4-effects-of-nuclear-weapon-testing-by-the-soviet-union/.

[9] Near-Earth Object Survey and Deflection Analysis of Alternatives, National Aeronautics and Space Administration, 2007, URL https://www.nasa.gov/pdf/171331main_NEO_report_march07.pdf.

[10] J.P. Sanchez, C. Colombo, M. Vasile, G. Radice, MUlticriteria Comparison Among Several Mitigation Strategies for Dangerous Near-Earth Objects, J. Guid. Control Dyn. (2009) http://dx.doi.org/10.2514/1.36774.

[11] R. Adams, J. Campbell, R. Hopkins, W.S. Smith, et al., Near Earth Object (NEO) Mitigation Options Using Exploration Technologies, National Aeronautics and Space Administration, 2007, URL https://ntrs.nasa.gov/citations/20070019778.

[12] R. Rhodes, D. Beller, The Need for Nuclear Power: Viewpoint on the World's Challenging Energy Future, International Atomic Energy Agency, 2000, URL https://www.iaea.org/sites/default/files/publications/magazines/bulletin/bull42-2/42204784350.pdf.

[13] M. Bruck Syal, D.S. Dearborn, P.H. Schultz, Limits on the use of nuclear explosives for asteroid deflection, Acta Astronaut. (2012) http://dx.doi.org/10.1016/j.actaastro.2012.10.025.

[14] K. Howley, R. Managan, J. Wasem, Blow-off momentum from melt and vapor in nuclear deflection scenarios, Lawrence Livermore National Laboratory, 2014, http://dx.doi.org/10.1016/j.actaastro.2014.06.022.

[15] D. Dearborn, S. Patenaude, R. Managan, The Use of Nuclear Explosives To Disrupt or Divert Asteroids, Lawrence Livermore National Laboratory, 2007, URL https://digital.library.unt.edu/ark:/67531/metadc890248/.

[16] B.J. Zimmerman, B. Wie, GPU-accelerated computational tool for studying the effectiveness of asteroid disruption techniques, Acta Astronaut. (2016) http://dx.doi.org/10.1016/j.actaastro.2016.06.023.

[17] T. Ahrens, A. Harris, Deflection and fragmentation of near-Earth asteroids, Nature (1992) http://dx.doi.org/10.1038/360429a0.
[18] D. Dearborn, M. Bruck Syal, B. Barbee, G. Gisler, K. Greenaugh, K. Howley, R. Leung, J. Lyzhoft, P. Miller, J. Nuth, C. Plesko, B. Seery, J. Wasem, R. Weaver, M. Zebenay, Options and uncertainties in planetary defense: Impulse-dependent response and the physical properties of asteroids, Acta Astronaut. (2020) http://dx.doi.org/10.1016/j.actaastro.2019.10.026.
[19] K. Howley, J. Wasem, D. Dearborn, R. Managan, P. Miller, Lower Limits on NEO Deflection Velocities from Melt and Vapor Blow-off Momentum, in: International Academy of Astronautics Planetary Defense Conference, 2013, URL https://iaaspace.org/wp-content/uploads/iaa/Scientific%20Activity/conf/pdc2013/IAA-PDC13-04-25.pdf.
[20] R. Managan, K. Howley, J. Wasem, Efficient and Accurate Mapping of Nuclear-Energy Deposition, in: 2015 Planetary Defense Conference, 2015, URL https://iaaspace.org/wp-content/uploads/iaa/Scientific%20Activity/conf/pdc2015/IAA-PDC-15-P-53.pdf.
[21] A. Ferguson, Analysis of Neutron Effects for Asteroid Disruption, Air Force Institute of Technology, 2016, URL https://scholar.afit.edu/etd/338/.
[22] J.C. Sanders, Near Earth Object Collisional Mitigation Via Intense Neutron and Photon Sources: a Study in Asteroid Interdiction and Energy Coupling (Oregon State University Honors Baccalaureate Thesis), 2006, URL https://ir.library.oregonstate.edu/concern/honors_college_theses/sq87bw34z?locale=en.
[23] J. Holdren, Office of Science and Technology Policy Letter on Near-Earth Objects to the House Committee on Science and Technology, White House Arch. (2010) URL https://obamawhitehouse.archives.gov/sites/default/files/microsites/ostp/ostp-letter-neos-house.pdf.
[24] D. Dearborn, 21st Century Steam for Asteroid Mitigation, Lawrence Livermore National Laboratory, 2004, http://dx.doi.org/10.2514/6.2004-1427.
[25] S.W. Mosher, et al., ADVANTG—An Automated Variance Reduction Parameter Generator, Oak Ridge National Laboratory, 2015, http://dx.doi.org/10.2172/1210162.
[26] K.S. Krane, Introductory Nuclear Physics, John Wiley & Sons Publishing, 1988.
[27] J.P. Lestone, Watt Parameters for the Los Alamos Model: Subroutine Getab, Los Alamos National Laboratory, 2007, URL https://arxiv.org/abs/1410.1769.
[28] D.T. Britt, D.K. Yeomans, K.R. Housen, G. Consolmagno, Asteroid Density, Porosity, and Structure, in: Asteroids III, University of Arizona Press, 2002, URL https://www.lpi.usra.edu/books/AsteroidsIII/pdf/3022.pdf.
[29] D. Pelowitz, MCNP6 User's Manual, Los Alamos National Security LLC, 2008.
[30] D. Brown, Evaluated Nuclear Data File (ENDF), Brookhaven National Laboratory, 2018, URL https://www.nndc.bnl.gov/exfor/endf00.jsp.
[31] A.L. Nichols III, D.M. Dawson, ALE3D User's Manual, Lawrence Livermore National Laboratory, 2018.
[32] P. Hammerling, J. Remo, NEO interaction with nuclear radiation, Acta Astronaut. (1995) http://dx.doi.org/10.1016/0094-5765(95)00111-5.
[33] J.E. Turner, Atoms, Radiation, and Radiation Protection, Wiley-VCH Publishing, 2007.
[34] E.W. Weisstein, Circle-Line Intersection, MathWorld, A Wolfram Web Resource, 2019, URL http://mathworld.wolfram.com/Circle-LineIntersection.html.
[35] Gamma decay, Encyclopædia Br. (1998) URL https://www.britannica.com/science/gamma-decay.
[36] E.Y. Aristova, A.A. Aushev, V.K. Baranov, I.A. Belov, S.A. Bel'kov, A.Y. Voronin, et al., Laser Simulations of the Destructive Impact of Nuclear Explosions on Hazardous Asteroids, J. Exp. Theor. Phys. (2018) http://dx.doi.org/10.1134/S1063776118010132.
[37] R. Weaver, P. Miller, K. Howley, et al., Los Alamos and Lawrence Livermore National Laboratories Code-to-Code Comparison of Inter Lab Test Problem 1 for Asteroid Impact Hazard Mitigation, Los Alamos National Laboratory, 2016, http://dx.doi.org/10.2172/1235218.
[38] P. Bedrossian, Neutrons and Granite: Transport and Activation, Lawrence Livermore National Laboratory, 2004, http://dx.doi.org/10.2172/15009828.
[39] D.B. Henry, The temperature of an asteroid, Ann. I.H.P. Phys. Théor. (1991) URL http://www.numdam.org/item/AIHPA_1991__55_2_719_0.
[40] M. Bruck Syal, J.M. Owen, C.D. Raskin, D.S. Dearborn, P.L. Miller, Integrated Blowoff and Breakup Calculations for Asteroid Deflection by Nuclear Ablation, in: International Academy of Astronautics 2017 Planetary Defense Conference, 2017, URL https://iaaweb.org/iaa/Scientific%20Activity/conf/pdc2017/IAA-PDC-17-04-01ab.pdf.
[41] B. Kaplinger, B. Wie, D. Dearborn, Nuclear fragmentation/dispersion modeling and simulation of hazardous near-Earth objects, Acta Astronaut. (2012) http://dx.doi.org/10.1016/j.actaastro.2012.10.013.
[42] P. Richet, Y. Bottinga, Thermochemical properties of silicate glasses and liquids: A review, Rev. Geophys. (1986) http://dx.doi.org/10.1029/RG024i001p00001.
[43] P. Chodas, Asteroid 2019 PDC Chance of Earth Impact Now 10%, in: 2019 Planetary Defense Conference, 2019, URL https://cneos.jpl.nasa.gov/pd/cs/pdc19/pdc19_briefing2.pdf.